

Resonant Nonlinear Synthetic Metasurface with Combined Phase and Amplitude Modulations

Bingxia Wang, Kai Wang,* Xuanmiao Hong, Yan Sheng, Shuhang Qian, and Peixiang Lu*

Nonlinear metasurfaces provide a promising platform for integrated nonlinear photonic devices owing to their unprecedented capability of nonlinear wavefront manipulation. However, the previously reported second-harmonic (SH) metasurfaces are mainly based on the nonlinear Pancharatnam–Berry phase modulation. While this method is quite convenient and robust, it shows limitations of modulation efficiency and the difficulty in extending to multidimensional combined modulations. Here, the resonant nonlinear synthetic metasurface is proposed and experimentally demonstrated for independent phase and amplitude modulations of the SH beam. A high SH modulation efficiency of 75% (with a theoretical limit of 90%) is achieved in the polarization-dependent SH metalens. Moreover, SH holographic imaging with phase and amplitude (at 2 and 4 levels) combined modulation is realized experimentally. Compared with the pure-phase modulation, the signal-to-noise ratios are increased by 2 and 3 times when 2- and 4-level amplitude controls are introduced. This is not only an important step in the improvement and innovation of holographic display technology, but also paves a distinct avenue toward multifunctional, higher efficiency, and ultracompact nonlinear optical devices.

consist of nanometer-sized plasmonic or all-dielectric nanoantenna, which are arranged in predesigned way in order to achieve a full-phase ($0-2\pi$) modulation.^[8–12] Previously reported works were mainly focused on the second- and third-harmonic (SH and TH) metasurfaces, demonstrating multifunctional manipulations of SH or TH beams, such as beam steering,^[1,13,14] optical vortex,^[15–17] metalens^[18–20] and holographic imaging.^[12,21–23] In particular, all of the SH metasurfaces reported so far are based on Pancharatnam–Berry (PB) phase.^[24,25] The PB schemes are quite simple and convenient with a robustness against fabrication errors, showing great potentials in various applications.^[1,17,18,26] However, they suffer from the low SH modulation efficiency (no more than 50% in theory) as well as the difficulty in extending to multidimensional combined modulations.^[27,28]

1. Introduction

Nonlinear metasurfaces have attracted extensive attentions in modern optics and nanophotonics due to their unique ability to generate light with a controlled wavefront at harmonic frequencies,^[1–3] which shows potential applications in quantum optics^[4,5] and optical communication.^[6,7] They commonly

In the field of linear metasurfaces,^[29–34] phase–amplitude combined modulation is capable of achieving more advanced functionalities than pure-phase modulation. Specifically, it significantly enhances the holographic imaging quality^[35,36] and shows great potentials in holographic display, virtual reality and augmented reality. Furthermore, it is able to realize many functionalities that are beyond reach by pure-phase modulation, such as 3D display, real color reproduction, and high-fidelity optical security devices.^[37–40] However, SH metasurface with phase–amplitude combined modulation requires that many strict constraints are satisfied simultaneously, such as resonance enhancement, frequency conversion, and phase–amplitude combined modulation of the SH beam. Therefore, it poses severe challenges in both physics and fabrications, which, to the best of our knowledge, is still an untouched area of research.


We have recently proposed the concept of nonlinear synthetic metasurface. It is composed of a plasmonic metasurface and transition metal dichalcogenides (TMDs) monolayer showing an efficient SH conversion efficiency (10^{-5} to 10^{-6}).^[27,41–44] More importantly, the modulation mechanism is completely different from that in the previous SH metasurfaces. The plasmonic metasurface acts as a phase modulator for the local-field of fundamental frequency while the TMDs monolayer acts as a highly efficient nonlinear material. Therefore, it provides a simple solution for the advanced SH wavefront manipulation without considering the above mentioned multiple strict

Dr. B. Wang, Prof. K. Wang, X. Hong, S. Qian, Prof. P. Lu
Wuhan National Laboratory for Optoelectronics and School of Physics
Huazhong University of Science and Technology
Wuhan 430074, China
E-mail: kale_wong@hust.edu.cn; lupeixiang@hust.edu.cn

Dr. Y. Sheng
Laser Physics Center
Research School of Physics
Australian National University
Canberra ACT 2601, Australia

Prof. P. Lu
CAS Center for Excellence in Ultra-Intense Laser Science
Shanghai 201800, China

Prof. P. Lu
Guangdong Intelligent Robotics Institute
Dongguan 523808, China

 The ORCID identification number(s) for the author(s) of this article can be found under <https://doi.org/10.1002/lpor.202100031>

DOI: 10.1002/lpor.202100031

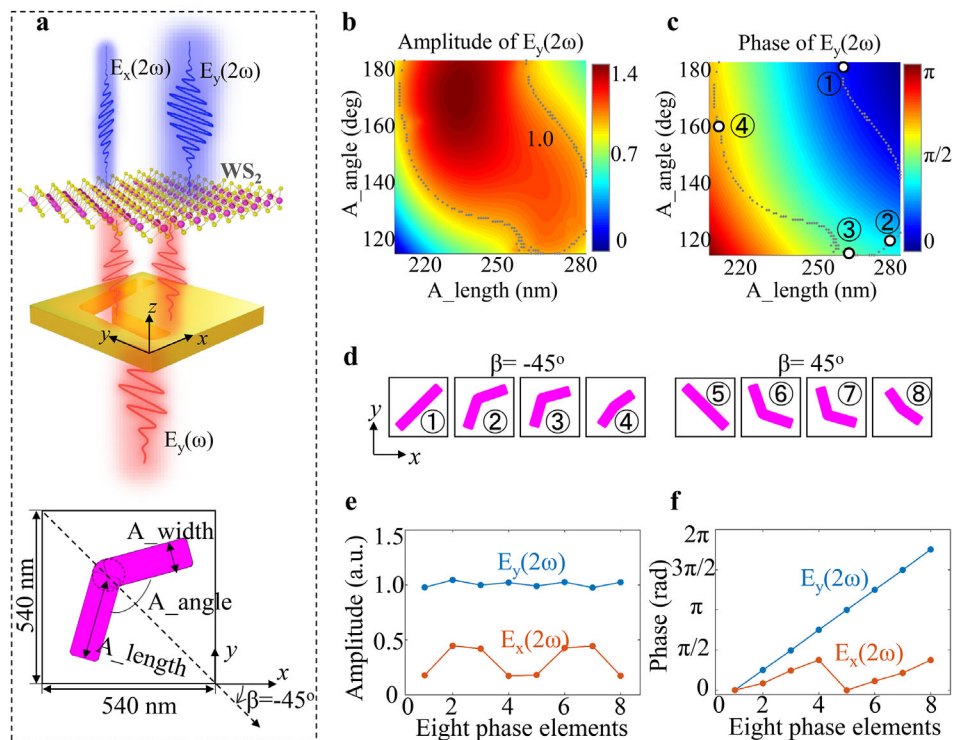


Figure 1. Design of V-shaped resonant nonlinear synthetic metasurface. a) Illustration of the structure and the operational mechanism of resonant nonlinear synthetic metasurface. The desired y -polarized SHG is modulated under an excitation of a y -polarized incident laser at wavelength of 810 nm. As a comparison, the x -polarized SHG, which is not the focus of this work, shows a much lower efficiency. b,c) The amplitudes and phases of the y -polarized SHG versus the arm-length (A_length) and the splitting-angle (A_angle) of the V-shaped synthetic structure. The dashed line is the contour line with amplitude of 1.0. The circles on the contour line indicate the parameters of the structures providing the discrete phases of $0, \pi/4, \pi/2$, and $3\pi/4$. d) The shapes of eight basic synthetic structures providing a constant amplitude of 1.0 but discrete phases of $0, \pi/4, \pi/2, 3\pi/4, \pi, 5\pi/4, 3\pi/2$, and $7\pi/4$. The comparison of amplitudes e) and phases f) of x - and y -polarized SHG from the eight basic structures.

constraints. In addition, V-shaped plasmonic nanohole array with double-resonance properties have been proved to be capable of independently controlling phase and amplitude in linear optics.^[45–47] Therefore, it inspires us to integrate the V-shaped plasmonic nanohole array with TMDs monolayer to realize the phase–amplitude combined modulation of SH waveform.

In this work, we experimentally demonstrate the independent phase and amplitude modulations of the SH beam based on the resonant nonlinear synthetic metasurface, which is consisted of the resonant V-shaped Au nanohole array and monolayer WS_2 . A high SH modulation efficiency up to 75% (90% in theory) is achieved in the polarization-dependent SH metalens, which is the highest value have ever been reported. Moreover, SH holographic imaging with phase and amplitude (at 2 and 4 levels) combined modulation is achieved. Compared with pure-phase modulation (1-level amplitude), the signal-to-noise ratios of the SH holographic imaging are increased by 2 and 3 times when 2- and 4-level amplitude control is introduced. This work extends the existing pure-phase modulation to 2D phase–amplitude combined modulation and offers new possibilities for complex electromagnetic field generation at harmonic frequencies. It is of great potential in the improvement and innovation of holographic display technology and paves a distinct avenue toward multifunctional, higher-efficiency and ultracompact nonlinear optical devices.

2. Results

The concept of resonant nonlinear synthetic metasurface for SH phase–amplitude combined modulation is illustrated in **Figure 1**. As shown in Figure 1a, one pixel of the metasurface is composed of a V-shaped Au nanohole and a WS_2 monolayer. With this synthetic structure, the y -polarized second harmonic generation (SHG) is modulated under a y -polarized excitation at wavelength of 810 nm. As a comparison, the x -polarized SHG, which is not the focus of this work, shows a much lower efficiency. The operational mechanism can be divided into two steps. First, the local-field of fundamental frequency with phase–amplitude combined modulation is obtained by interactions of the incident field with V-shaped nanoholes with different arm-length and splitting-angle. And then, the local-field of fundamental frequency further excites the attached WS_2 monolayer for generating SH signal. The insert shows the projection view of the synthetic structure with size of $540 \times 540 \text{ nm}^2$. The parameters of this structure are illustrated as follows: the length and width of the two arms are A_length and A_width ; the diameter of the circle connecting both arms is A_width ; the angle between both arms is A_angle ; the angle between symmetry axis and x -axis is β , where $\beta = -45^\circ$ in this case; the thickness of the Au nanohole is 60 nm. During the design, we fixed the arm-width as 100 nm according to our fabrication resolution in practical,

while the design parameters (namely A_length and A_angle) are varied over a wide range in order to realize multilevel amplitude and full-phase combined modulations.

The numerical simulation of the generated SH electric-field can be split into two steps. First, a full-wave simulation of the local-field of fundamental frequency in the V-shaped nanohole is performed by using the finite element method with COMSOL Multiphysics software. And then, the calculated local-field is used to pump the attached WS_2 monolayer for frequency conversion calculated with MATLAB software. Figure 1b,c displays the amplitudes and phases of γ -polarized SHG as function of the A_length and A_angle . The dashed line in Figure 1b represents the contour line at 70% of the maximum amplitude. For convenience, we set the amplitude value on this contour line as 1.0. The dashed line in Figure 1c indicates that V-shaped synthetic structures with different shapes give SH phases ranging from 0 to π while keeping the amplitude as a constant of 1.0. Structures (①, ②, ③, ④) depicted as circles on the amplitude contour line provide four discrete phases (0, $\pi/4$, $\pi/2$, and $3\pi/4$) with $\beta = -45^\circ$. The shapes of these four structures are displayed in the left panel of Figure 1d. Another four structures (⑤, ⑥, ⑦, ⑧) have the same design parameters as the counterpart on the left but with $\beta = 45^\circ$, which provide the relative phase shifts of π , $5\pi/4$, $3\pi/2$, and $7\pi/4$, respectively.

The numerically calculated amplitudes and phases of the γ -polarized SHG for $\beta = -45^\circ$ and $\beta = 45^\circ$ are summarized in Figure S1 (Supporting Information). The detailed parameter values of these eight basic synthetic structures in Figure 1d are listed in Table S1 (Supporting Information). The numerically calculated local field of fundamental frequency are shown in Figure S2 (Supporting Information). According to the symmetry of WS_2 monolayer, the calculated SH local field are presented in Figure S3 (Supporting Information). To describe the polarization state of the emitted SHG, Stokes parameters (I , Q , U , and V) are calculated with the SHG in Figure S3 (Supporting Information). $I = 1$ is the normalized total SH intensity; Q is the light component along x -polarization direction; U is the light component polarized at 45° to the x -axis; V is the right circularly polarized light component. Then, the degree of polarization (P) can be calculated with formula $P = \sqrt{Q^2 + U^2 + V^2}/I$. The Q , U , V , and P parameters are displayed in Figure S4 (Supporting Information). $P = 1$ indicates the complete polarization of the emitted SHG. Therefore, the total SHG can be divided into x - and γ -polarized components. These two orthogonal polarization components are extracted, and then the averaged amplitude and phase are plotted in Figure 1e,f. It shows these eight basic structures provide a full phase control on the emitted γ -polarized SHG. Here, we define the modulation efficiency as the ratio between the target SH (γ -polarized SH in this case) intensity and the total SH intensity, which can be written as

$$\eta_M = \frac{I_y(2\omega)}{I_{total}(2\omega)} = \frac{I_y(2\omega)}{I_x(2\omega) + I_y(2\omega)} \quad (1)$$

With the data presented in Figure 1e the theoretically averaged modulation efficiency of γ -polarized SHG can be up to 92% according to Equation (1).

In the following, we use these eight basic structures as building blocks to construct phase plate for an arbitrary SH wavefront

shaping. We design a phase plate to realize SH metalens with focal length of $f = 50 \mu\text{m}$. The schematic representation of the experimental setup is shown in Figure S5 (Supporting Information). To generate the desired focusing, the required SH phase, $\varphi(x,y)$ can be written as

$$\varphi(x,y) = \frac{2\pi(f - \sqrt{x^2 + y^2 + f^2})}{\lambda} \quad (2)$$

where λ is the SH wavelength. With Equation (2) the calculated phase $\varphi(x,y)$ varies continuously from 0 to 2π , so we divide it into eight discrete values. Then, the discrete phase distribution is plotted in the left insert of Figure 2a. The metasurface can be designed by encoding these eight discrete phase values with the eight basic structures as displayed in the bottom insert. The designed Au nanohole array is shown in Figure 2a and each V-shaped nanohole can be clearly seen from the enlarged pattern at the marked white area. Figure 2b displays the scanning electron microscope image of the nanohole array fabricated by focused ion beam (FIB). It can be clearly seen that the enlarged and eight basic structures in the marked area are in good agreement with the theoretical designs. It is worth mentioning that this metasurface has 2828 pixels in total and the size of each pixel is $540 \times 540 \text{ nm}^2$.

Figure 2c displays the optical image of the fabricated resonant nonlinear synthetic metasurface consisting of Au nanohole array and a WS_2 monolayer. The line connected to the circular nanohole array is used to indicate the direction of the array coordinate system. The angle between crystal coordinate (x_c, y_c) and array coordinate (x_a, y_a) is marked as φ . Since WS_2 monolayer has $P63/mmc$ crystal symmetry, the deviation angle (φ) between the crystal axis and the array axis causes the outgoing γ -polarized SHG to rotate 3φ around the array axis accordingly.^[48] Figure 2d demonstrates the SH intensity emitted from the circular sample is stronger than that from the bare monolayer WS_2 . The recorded spectral property of the generated SH signals from Au/ WS_2 metasurface (blue line) and bare monolayer WS_2 (red line) under 90 mW excitation laser are presented in Figure 2e. It shows a 4-times SH enhancement factor from Au/ WS_2 metasurface in comparison with the bare monolayer WS_2 , which is due to the resonance enhancement of the V-shaped nanoholes. In addition, the calculation method of SH signal from resonant nonlinear synthetic metasurface is discussed in Section S1 (Supporting Information). The comparison of SH phase and amplitude modulated with this resonant metasurface and the previous PB phase metasurface^[27,41] under the same input intensity is presented in Figure S6 (Supporting Information). Besides, the numerically calculated γ -polarized SHG amplitude distribution from eight basic structures under γ -polarized excitation with three different wavelengths are illustrated in Figure S7 (Supporting Information). High conversion efficiency is an outstanding feature of this Au/ WS_2 synthetic metasurface. Specifically, V-shaped Au nanoholes are used to modulate the phase and amplitude of the FF field; WS_2 is used as an efficient frequency converter with a second-order susceptibility as large as $\approx 4.5 \text{ nm V}^{-1}$.^[48] Besides, the V-shaped Au nanoholes can be optimized to resonate with the FF field, so as to further boost the SH conversion efficiency. The experimentally measured SHG conversion

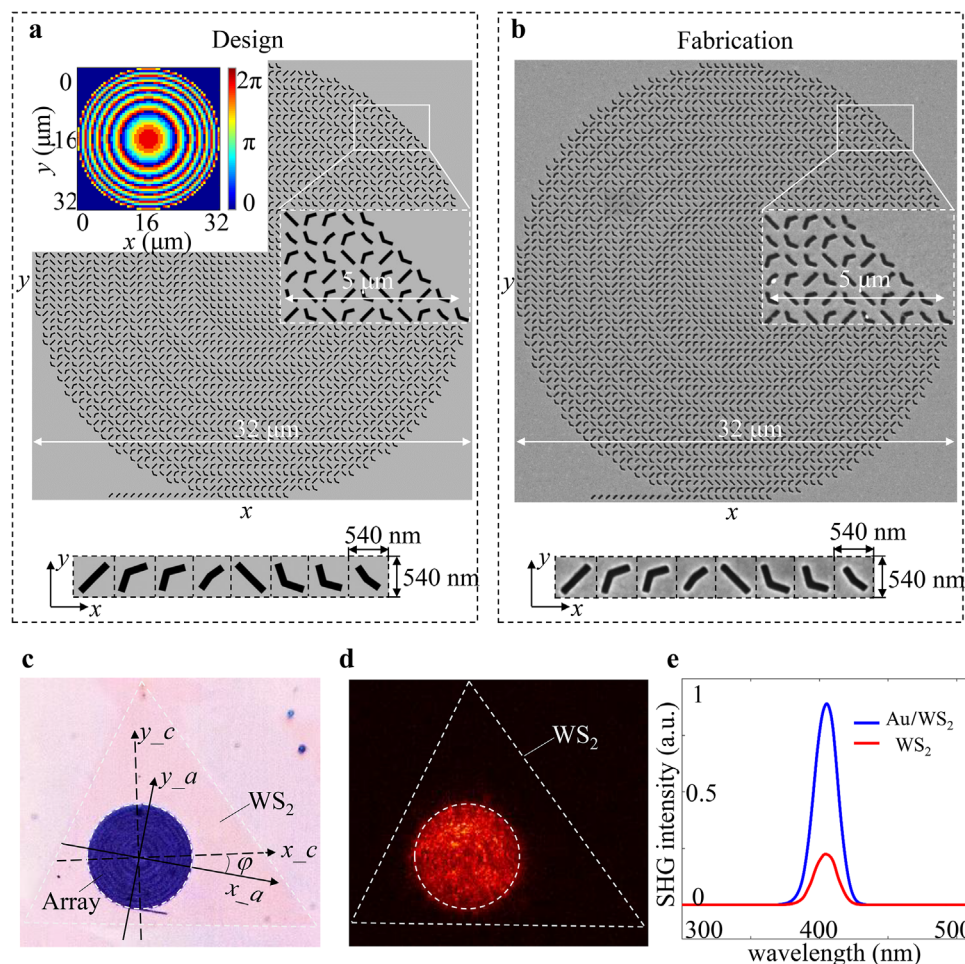


Figure 2. Design of SH metalens with a focal length of 50 μm . a) The designed V-shaped Au nanohole array according to the calculated phase distribution in the upper insert. An expanded view of Au nanoholes in the marked area and the eight basic structures are also shown in the insert. b) The Au nanohole array fabricated by FIB method. The inserts give an expanded view of the nanoholes in the marked area and the eight basic structures. c) The optical microscope image of the resonant nonlinear synthetic metasurface consisting of V-shaped Au nanohole array and WS_2 monolayer; the angle between crystal coordinate and array coordinate is marked as φ . d) The SH intensity distribution at the sample plane detected by CCD. e) The spectra of total SH signals from Au/ WS_2 synthetic metasurface (blue curve) and a bare monolayer WS_2 (red curve).

efficiency is of the order of 10^{-6} , which can be further enhanced by stacking multilayer WS_2 along the same crystal direction.^[49]

Figure 3 presents the polarization-dependent SH metalens. The measured γ - and x -polarized SHG evolution along the z -axis under the γ -polarized excitation are shown in Figure 3a,b. The top inserts present the distribution of γ - and x -polarized SHG at $z = 0 \mu\text{m}$. Obviously, the intensity of γ -polarized SHG is stronger than that of x -polarized SHG. By integrating the total SH intensity, the SH modulation efficiency is determined to be 75%. The bottom inserts present the corresponding SH distribution with γ - and x -polarization at the focal plane ($z = 52 \mu\text{m}$). It can be seen that the γ -polarized SHG shows a clear focus spot with a diameter of $\approx 1 \mu\text{m}$, while no focus effect for the x -polarized SHG. This indicates that the SH metalens has an effective manipulation on the γ -polarized SHG, which is consistent with the theoretical design. Accordingly, Figure 3c,d presents the numerically simulated evolution of γ - and x -polarized SHG intensity along the z -axis. The calculated γ - and x -polarized SHG intensities at $z = 0 \mu\text{m}$ are shown in the upper inserts, indicating

a high SH modulation efficiency up to 90%. The lower inserts show an intensive focusing spot at $z = 50 \mu\text{m}$ with a diameter around $1 \mu\text{m}$ for γ -polarized SHG while x -polarized SHG is not modulated, in good agreement with the experimental results. This high SH modulation efficiency benefits from the smart design of our proposed synthetic metasurface, with which both the x - and γ -polarized FF fields can be used to excite WS_2 and contribute to the desired γ -polarized SHG. More details are provided in Section S2 (Supporting Information).

High-quality holographic imaging at harmonic frequency is also demonstrated by introducing the amplitude modulation (at 2 and 4 levels). As shown in **Figure 4a**, the amplitude of γ -polarized SHG can be continuously tuned by changing A_{length} and A_{angle} (taking the branch of $\beta = -45^\circ$ for example). In order to keep consistent with the amplitude in Figure 1, the amplitude value on the green dashed contour line is set as $A_1 = 1.0$. Then, the contour lines with amplitudes of $A_2 = 0.75$, $A_3 = 0.5$ and $A_4 = 0.25$ are plotted with red, black and pink dashed lines, respectively. Furthermore, Figure 4b presents the phase at each

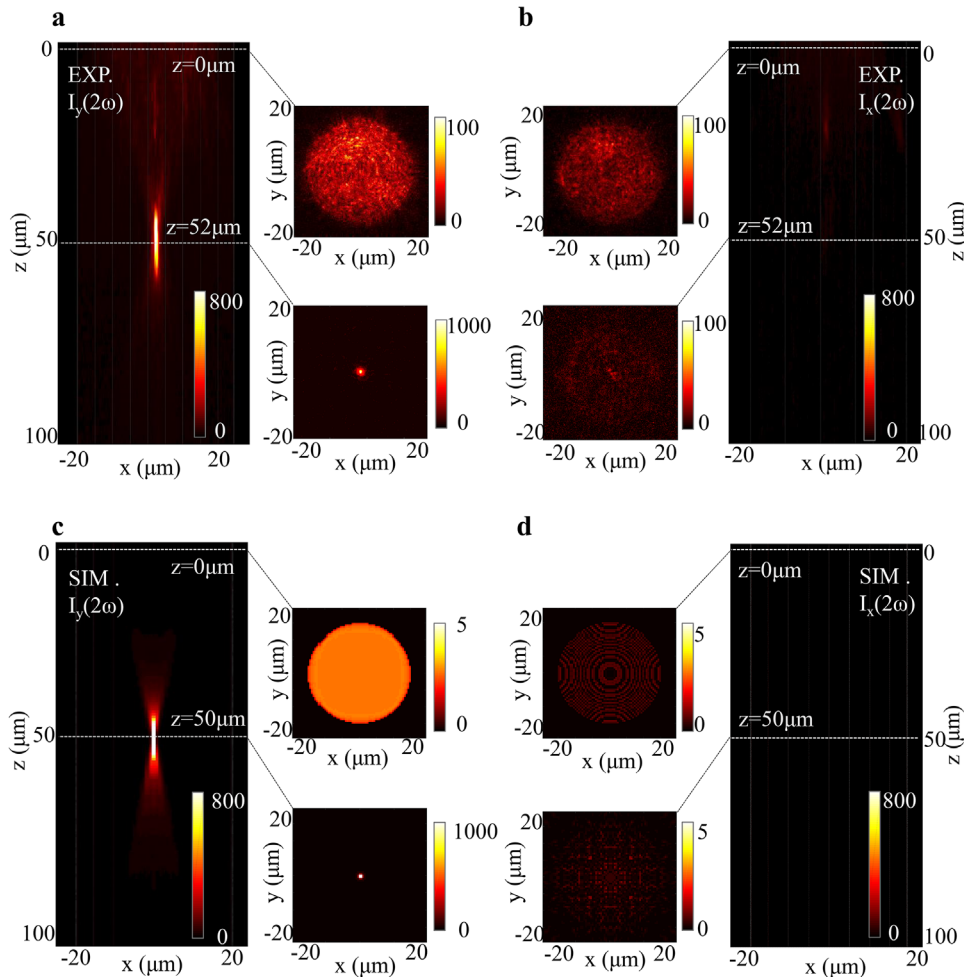


Figure 3. SHG intensity evolution along propagation z -axis. a,b) Experimentally measured y - and x -polarized SHG intensity evolution under an excitation of a y -polarized laser. It shows an intensive focusing effect at $z = 52 \mu\text{m}$ for y -polarized SHG while there is no focusing for x -polarized SHG. The y - and x -polarized SHG intensity at $z = 0 \mu\text{m}$ is used to calculate the SH manipulation efficiency, which is up to 75%. c,d) Numerically calculated y - and x -polarized SHG intensity evolution. It shows an intensive focusing effect at $z = 50 \mu\text{m}$ for y -polarized SHG while there is no focusing for x -polarized SHG. The y - and x -polarized SHG intensity at $z = 0 \mu\text{m}$ indicate the numerically calculated manipulation efficiency is up to 90%.

level of SH amplitude ranges from 0 to π . In the map, four groups of discrete phases of $0, \pi/4, \pi/2,$ and $3\pi/4$ are marked with circles ($A_1 = 1$), stars ($A_2 = 0.75$), squares ($A_3 = 0.5$), and triangles ($A_4 = 0.25$), respectively. The corresponding shapes of the synthetic structures are as shown on the left side of Figure 4c. The right side of Figure 4c shows the structures with the same parameters but at $\beta = 45^\circ$, providing the relative phase shifts of $\pi, 5\pi/4, 3\pi/2,$ and $7\pi/4$. The numerically calculated maps of amplitude and phase of the y -polarized SHG at $\beta = -45^\circ$ and $\beta = 45^\circ$ are summarized in Figure S8 (Supporting Information). The detailed design parameter values of these synthetic structures with amplitudes ($A_1, A_2, A_3,$ and A_4) are listed in Table S2 (Supporting Information). The calculated SH local-field from these structures are shown in Figure S9 (Supporting Information). Figure 4d,e shows the calculated amplitude and phase of y -polarized SHG from the corresponding structures in Figure 4c. Obviously, the SH amplitude is discretized into 4 levels (1.0, 0.75, 0.5, and 0.25), while the phase at each level ranges from 0 to 2π . It indicates that the phase–amplitude combined modulation can be realized

based on the Au/WS₂ resonant nonlinear synthetic metasurface. In addition, Figure S10 (Supporting Information) further indicates that the amplitude–phase combined modulation is quite robust.

For a clear comparison of SH holographic imaging, we have prepared three samples to perform phase–amplitude combined modulation at 1-level (Sample 1), 2-level (Sample 2) and 4-level (Sample 3) amplitude control, while maintaining the same target image of “UFO” (abbreviation for ultrafast optics). Figure 5a shows the illustration of the SH holographic imaging. Specifically, the emitted y -polarized SHG is designed to image in the Fresnel region under a y -polarized excitation, the image plane is designed to be $200 \mu\text{m}$ from the sample and each letter in the pattern is $25 \mu\text{m}$ wide. The SH amplitude and phase at hologram plane can be calculated using the iterative split-step fast Fourier transform beam propagation method (SS-FFT-BPM)^[50] (see Section S3 in the Supporting Information). The calculated SH amplitude and phase at hologram plane for Samples 1, 2 and 3 are shown in the left, middle and right column of Figure 5b.

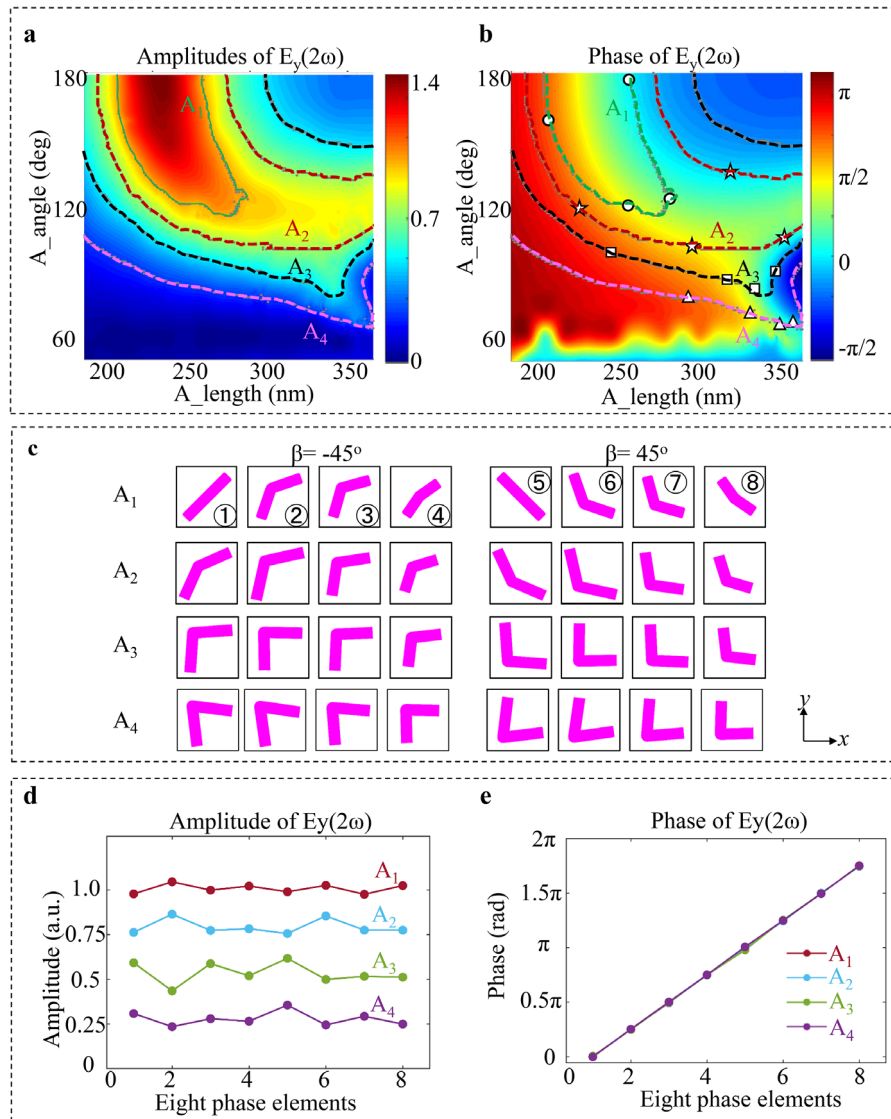


Figure 4. Design of synthetic metasurface for phase and multilevel-amplitude combined modulation. The amplitudes a) and phases b) of the γ -polarized SHG versus the arm-length (A_length) and the splitting-angle (A_angle) of the V-shaped synthetic structure. The dashed lines are the contour lines with four-level amplitude of 0.25, 0.5, 0.75, and 1.0. The circles, stars, squares, and triangles on the contour lines indicate the parameter of the structures providing phase shifts of $0, \pi/4, \pi/2$, and $3\pi/4$. c) Demonstration of the four groups of basic synthetic structures providing discrete phases of $0, \pi/4, \pi/2, 3\pi/4, \pi, 5\pi/4, 3\pi/2$, and $7\pi/4$. The averaged amplitude d) and phase e) of γ -polarized SHG from these four groups of basic structures.

Sample 1 is designed by properly arranging the positions of eight basic synthetic structures with amplitude A_1 , which is used for pure-phase (1-level amplitude) modulation; Sample 2 is based on 16 basic synthetic structures (with amplitudes A_1 and A_3) for 2-level amplitude and phase combined modulations; Sample 3 is based on 32 basic synthetic structures (with amplitudes A_1, A_2, A_3 , and A_4) for 4-level amplitude and phase combined modulations. It is worth mentioning that each designed and fabricated sample, as shown in Figure S11 (Supporting Information), contains 5024 pixels in total with the size of each pixel of $540 \times 540 \text{ nm}^2$.

The left, middle and right columns in Figure 5c presents the γ -polarized SHG intensity distribution from Samples 1, 2 and 3. Top row represents the simulated results using the SS-

FFT-BPM.^[50] Bottom row shows the experimentally measured results, which are in good agreement with the simulations. Notably, as the levels of the amplitude modulation is increased, the noise of holographic imaging is dramatically decreased. We define the signal-to-noise ratio (SNR) as $P_{\text{signal}}/P_{\text{noise}} = P_{\text{signal}}/(P_{\text{total}} - P_{\text{signal}})$, where P_{total} and P_{signal} are the total power and pure signal power. P_{total} is obtained by calculating the total integrated intensity in Figure 5c, while P_{signal} can be obtained by calculating the integrated intensity of the UFO-shaped SH holographic image. The numerically calculated and experimentally measured SNR for these three samples are (2.2, 3.0, and 4.0) and (0.7, 1.4, and 2.3), respectively. In addition, the experimental results show more noises than the simulation results, which is mainly ascribed to the practical manufacturing errors.

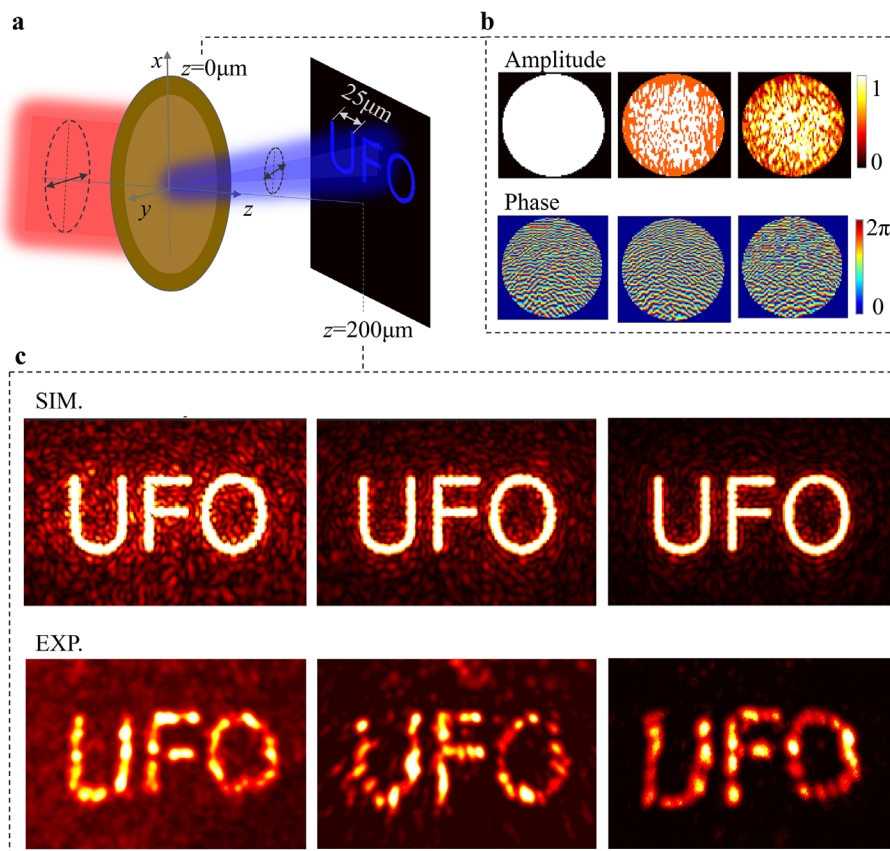


Figure 5. Demonstration of the impact of amplitude modulation on holographic imaging. a) Schematic illustration of y -polarized SH holographic imaging of “UFO” in the Fresnel region under an excitation of a y -polarized laser. b) Left, middle, and right: The calculated y -polarized SHG amplitudes and phases at hologram plane for Sample 1 (1-level amplitude), Sample 2 (2-level amplitude), and Sample 3 (4-level amplitude). c) Left, middle, and right: The numerically simulated and experimentally measured y -polarized SHG intensity distributions from Samples 1–3. Clearly, as the amplitude modulation level increases, the quality of holographic imaging dramatically improves.

3. Discussion

In conclusion, we proposed and experimentally demonstrated the resonant nonlinear synthetic metasurface for SH phase–amplitude combined modulation. Our structure consists of the resonant V-shaped Au nanohole array and a monolayer WS_2 . It employs the advanced wavefront manipulation methods developed in linear optics to independently control the phase and amplitude. Furthermore, it takes the advantage of high-efficient nonlinear optical parametric process in WS_2 to directly transmit the controlled fundamental frequency to SHG. The result of polarization-dependent SH metalens indicates the manipulated SHG achieves a high modulation efficiency up to 90% in theory and 75% in experiment. Moreover, we performed phase and amplitude (at 2 and 4 levels) combined modulation of SH wavefront. Compared with pure-phase modulation (1-level amplitude), the SNR of SH holographic imaging increases by 2 and 3 times with 2- and 4-level amplitude modulation. This SH phase–amplitude combined modulation technology extends the current pure-phase modulation to simultaneous and independent phase and amplitude modulations offering new possibilities for complex electromagnetic field generation at new frequencies. It is of great potential applications in 3D display, optical encryption, data storage, etc.

Supporting Information

Supporting Information is available from the Wiley Online Library or from the author.

Acknowledgements

This work was supported by the National Natural Science Foundation of China (Nos. 91850113, 11774115, 12021004, and 11904271), the National Basic Research Program of China (973 Program) under grant 2014CB921301, the Basic and Applied Basic Research Major Program of Guangdong Province (No. 2019B030302003), and the Postdoctoral Science and Technology Activities Preferred Financing Project in Hubei Province. Special thanks to the Analytical and Testing Center of HUST and the Center of Micro-Fabrication and Characterization (CMFC) of WNLO for using their facilities. Thanks to the facility support of the Center for Nanoscale Characterization and Devices (CNCD), WNLO of HUST, and the Center of Nano-Science and Technology of Wuhan University for their support of sample fabrication.

Conflict of Interest

The authors declare no conflict of interest.

Author Contributions

K.W., B.X.W., and P.X.L. conceived the project. B.X.W. proposed the algorithm to perform the phase–amplitude combined modulation. B.X.W.

and X.M.H. designed the numerical simulations. B.X.W. performed the experiments. K.W., Y.S., and P.X.L. analyzed data and discussed the results. B.X.W. drafted the paper with the inputs from all authors. The manuscript was written through contributions of all authors. All authors have given approval to the final version of the manuscript.

Data Availability Statement

The data that support the findings of this study are available from the corresponding author upon reasonable request.

Keywords

nonlinear wavefront shaping, plasmonics nanohole array, second-harmonic generation, synthetic metasurface, transition metal dichalcogenides

Received: January 22, 2021

Revised: March 22, 2021

Published online:

- [1] G. Li, S. Chen, N. Polchaj, B. Reineke, P. W. H. Wong, E. Y. B. Pun, K. W. Cheah, T. Zentgraf, S. Zhang, *Nat. Mater.* **2015**, *14*, 607.
- [2] S. Liu, P. P. Vabishchevich, A. Vaskin, J. L. Reno, G. A. Keeler, M. B. Sinclair, I. Staude, I. Brener, *Nat. Commun.* **2018**, *9*, 2507.
- [3] H. Liu, C. Guo, G. Vampa, J. L. Zhang, T. Sarmiento, M. Xiao, P. H. Bucksbaum, J. Vučković, S. Fan, D. A. Reis, *Nat. Phys.* **2018**, *14*, 1006.
- [4] A. Valencia, A. Ceré, X. Shi, G. Molina-Terriza, J. P. Torres, *Phys. Rev. Lett.* **2007**, *99*, 243601.
- [5] R. Fickler, R. Lapkiewicz, W. N. Plick, M. Krenn, C. Schaeff, S. Ramelow, A. Zeilinger, *Science* **2012**, *338*, 640.
- [6] J. Wang, J. Y. Yang, I. M. Fazal, N. Ahmed, Y. Yan, H. Huang, Y. Ren, Y. Yue, S. Dolinar, M. Tur, A. E. Willner, *Nat. Photonics* **2012**, *6*, 488.
- [7] O. Tzang, A. M. Caravaca-Aguirre, K. Wagner, R. Piestun, *Nat. Photonics* **2018**, *12*, 368.
- [8] E. Almeida, G. Shalem, Y. Prior, *Nat. Commun.* **2016**, *7*, 10367.
- [9] N. Meinzer, W. L. Barnes, I. R. Hooper, *Nat. Photonics* **2014**, *8*, 889.
- [10] D. Lin, P. Fan, E. Hasman, M. L. Brongersma, *Science* **2014**, *345*, 298.
- [11] A. Arbabi, Y. Horie, M. Bagheri, A. Faraon, *Nat. Nanotechnol.* **2015**, *10*, 937.
- [12] W. Ye, F. Zeuner, X. Li, B. Reineke, S. He, C. W. Qiu, J. Liu, Y. Wang, S. Zhang, T. Zentgraf, *Nat. Commun.* **2016**, *7*, 11930.
- [13] D. Wei, C. Wang, H. Wang, X. Hu, D. Wei, X. Fang, Y. Zhang, D. Wu, Y. Hu, J. Li, S. Zhu, M. Xiao, *Nat. Photonics* **2018**, *12*, 596.
- [14] J. Bar-David, U. Levy, *Nano Lett.* **2019**, *19*, 1044.
- [15] S. Keren-Zur, O. Avayu, L. Michaeli, T. Ellenbogen, *ACS Photonics* **2015**, *3*, 117.
- [16] L. Wang, S. Kruk, K. Koshelev, I. Kravchenko, B. Luther-Davies, Y. Kivshar, *Nano Lett.* **2018**, *18*, 3978.
- [17] G. Li, L. Wu, K. F. Li, S. Chen, C. Schlickriede, Z. Xu, S. Huang, W. Li, Y. Liu, E. Y. B. Pun, T. Zentgraf, K. W. Cheah, Y. Luo, S. Zhang, *Nano Lett.* **2017**, *17*, 7974.
- [18] M. Tymchenko, J. S. Gomez-Diaz, J. Lee, N. Nookala, M. A. Belkin, A. Alù, *Phys. Rev. Lett.* **2015**, *115*, 207403.
- [19] Z. Nature Nanotechnology Adv. Funct. Mater. Li, W. Liu, Z. Li, C. Tang, H. Cheng, J. Li, X. Chen, S. Chen, J. Tian, *Laser Photonics Rev.* **2018**, *12*, 1800164.
- [20] C. Schlickriede, N. Waterman, B. Reineke, P. Georgi, G. Li, S. Zhang, T. Zentgraf, *Adv. Mater.* **2018**, *30*, 1703843.
- [21] F. Walter, G. Li, C. Meier, S. Zhang, T. Zentgraf, *Nano Lett.* **2017**, *17*, 3171.
- [22] E. Almeida, O. Bitton, Y. Prior, *Nat. Commun.* **2016**, *7*, 12533.
- [23] B. Reineke, B. Sain, R. Zhao, L. Carletti, B. Liu, L. Huang, C. De Angelis, T. Zentgraf, *Nano Lett.* **2019**, *19*, 6585.
- [24] M. V. Berry, *J. Mod. Opt.* **1987**, *34*, 1401.
- [25] F. J. Garcia-Vidal, E. Moreno, J. A. Porto, L. Martin-Moreno, *Phys. Rev. Lett.* **2005**, *95*, 103901.
- [26] S. Chen, F. Zeuner, M. Weismann, B. Reineke, G. Li, V. K. Valev, K. W. Cheah, N. C. Panoiu, T. Zentgraf, S. Zhang, *Adv. Mater.* **2016**, *28*, 2992.
- [27] G. Hu, X. Hong, K. Wang, J. Wu, H.-X. Xu, W. Zhao, W. Liu, S. Zhang, F. Garcia-Vidal, B. Wang, P. Lu, C.-W. Qiu, *Nat. Photonics* **2019**, *13*, 467.
- [28] K. Konishi, T. Higuchi, J. Li, J. Larsson, S. Ishii, M. Kuwata-Gonokami, *Phys. Rev. Lett.* **2014**, *112*, 135502.
- [29] G. Zheng, H. Mühlenbernd, M. Kenney, G. Li, T. Zentgraf, S. Zhang, *Nat. Nanotechnol.* **2015**, *10*, 308.
- [30] L. Wang, S. Kruk, H. Tang, T. Li, I. Kravchenko, D. N. Neshev, Y. S. Kivshar, *Optica* **2016**, *3*, 1504.
- [31] K. Huang, H. Liu, F. J. Garcia-Vidal, M. Hong, B. Luk'Yanchuk, J. Teng, C. W. Qiu, *Nat. Commun.* **2015**, *6*, 7059.
- [32] H. Butt, Y. Montelongo, T. Butler, R. Rajasekharan, Q. Dai, S. G. Shiva-Reddy, T. D. Wilkinson, G. A. J. Amaratunga, *Adv. Mater.* **2012**, *24*, OP331.
- [33] X. Zang, H. Ding, Y. Intaravanne, L. Chen, Y. Peng, J. Xie, Q. Ke, A. V. Balakin, A. P. Shkurinov, X. Chen, Y. Zhu, S. Zhuang, *Laser Photonics Rev.* **2019**, *13*, 1900182.
- [34] X. Zang, F. Dong, F. Yue, C. Zhang, L. Xu, Z. Song, M. Chen, P. Y. Chen, G. S. Buller, Y. Zhu, S. Zhuang, W. Chu, S. Zhang, X. Chen, *Adv. Mater.* **2018**, *30*, 1707499.
- [35] Y. Mu, M. Zheng, J. Qi, H. Li, J. Qiu, *Nanophotonics* **2020**, *9*, 4749.
- [36] L. Huang, S. Zhang, T. Zentgraf, *Nanophotonics* **2018**, *7*, 1169.
- [37] A. C. Overvig, S. Shrestha, S. C. Malek, M. Lu, A. Stein, C. Zheng, N. Yu, *Light: Sci. Appl.* **2019**, *8*, 92.
- [38] K. T. P. Lim, H. Liu, Y. Liu, J. K. W. Yang, *Nat. Commun.* **2019**, *10*, 252019.
- [39] Y. Bao, Y. Yu, H. Xu, C. Guo, J. Li, S. Sun, Z. K. Zhou, C. W. Qiu, X. H. Wang, *Light: Sci. Appl.* **2019**, *8*, 95.
- [40] L. Liu, X. Zhang, M. Kenney, X. Su, N. Xu, C. Ouyang, Y. Shi, J. Han, W. Zhang, S. Zhang, *Adv. Mater.* **2014**, *26*, 5031.
- [41] J. Chen, K. Wang, H. Long, X. Han, H. Hu, W. Liu, B. Wang, P. Lu, *Nano Lett.* **2018**, *18*, 1344.
- [42] X. Hong, G. Hu, G. Hu, W. Zhao, K. Wang, S. Sun, R. Zhu, R. Zhu, J. Wu, W. Liu, K. P. Loh, A. T. S. Wee, A. T. S. Wee, B. Wang, A. AlÀ, C. W. Qiu, P. Lu, P. Lu, *Research* **2020**, *2020*, 9085782.
- [43] W. Zhao, K. Wang, X. Hong, B. Wang, X. Han, H. Long, B. Wang, P. Lu, *Nanoscale* **2020**, *12*, 13330.
- [44] W. Zhao, K. Wang, X. Hong, B. Wang, X. Han, K. Wang, W. Liu, H. Long, B. Wang, P. Lu, *Sci. Bull.* **2021**, *66*, 449.
- [45] N. Yu, P. Genevet, M. A. Kats, F. Aieta, J. P. Tetienne, F. Capasso, Z. Gaburro, *Science* **2011**, *334*, 333.
- [46] X. Ni, N. K. Emani, A. V. Kildishev, A. Boltasseva, V. M. Shalaev, *Science* **2012**, *335*, 427.
- [47] X. Ni, A. V. Kildishev, V. M. Shalaev, *Nat. Commun.* **2013**, *4*, 2807.
- [48] C. Janisch, Y. Wang, D. Ma, N. Mehta, A. L. Elias, N. Perea-López, M. Terrones, V. Crespi, Z. Liu, *Sci. Rep.* **2014**, *4*, 5530.
- [49] Z. Zeng, X. Sun, D. Zhang, W. Zheng, X. Fan, M. He, T. Xu, L. Sun, X. Wang, A. Pan, *Adv. Funct. Mater.* **2019**, *29*, 1806874.
- [50] M. Scalora, M. E. Crenshaw, *Opt. Commun.* **1994**, *108*, 191.